AGU ADVANCING EARTH AND SPACE SCIENCES

Space Weather

RESEARCH ARTICLE
10.1029/2024SW004180

Data-Driven Transfer Functions From Differential Magnetometer Measurements to Enhance GIC Model Validation Capability: A Case Study in the Spanish Power Grid

S. Marsal[1], J. M. Torta[1], A. Martí[2], R. Hafizi[2], P. Piña-Varas[2], A. Marcuello[2], J. Ledo[3], J. J. Curto[1], P. Queralt[2], O. Cid[1], and M. Ibañez[1]

[1]Observatori de l'Ebre, (OE), University Ramon Llull - CSIC, Roquetes, Spain, [2]Department Dinàmica de la Terra i de l'Oceà, Institut Geomodels, Universitat de Barcelona, Barcelona, Spain, [3]Departamento de Física de la Tierra y Astrofísica, Universidad Complutense de Madrid, Madrid, Spain

Key Points:

- We update the validation of the geomagnetically induced current modeling in Spain using differential magnetometer measurements
- We describe a method based on transfer functions (TF) to derive diverse outputs from geomagnetic observatory data
- The TF are effective in reproducing the reference magnetometer data from Differential Magnetometer Method stations

Supporting Information:

Supporting Information may be found in the online version of this article.

Correspondence to:

J. M. Torta,
jmtorta@gencat.cat

Citation:

Marsal, S., Torta, J. M., Martí, A., Hafizi, R., Piña-Varas, P., Marcuello, A., et al. (2025). Data-driven transfer functions from differential magnetometer measurements to enhance GIC model validation capability: A case study in the Spanish power grid. *Space Weather*, *23*, e2024SW004180. https://doi.org/10.1029/2024SW004180

Received 23 SEP 2024
Accepted 16 FEB 2025

Author Contributions:

Conceptualization: S. Marsal, J. M. Torta, A. Martí, A. Marcuello, J. Ledo
Data curation: S. Marsal, J. M. Torta, P. Piña-Varas, A. Marcuello, J. Ledo
Formal analysis: S. Marsal, J. M. Torta, J. Ledo
Funding acquisition: S. Marsal, J. M. Torta, A. Martí, A. Marcuello
Investigation: S. Marsal, J. M. Torta, A. Martí, R. Hafizi, A. Marcuello, J. Ledo
Methodology: S. Marsal, J. M. Torta, A. Marcuello, J. Ledo

Abstract Geomagnetically induced currents (GICs) are unwanted currents flowing in long grounded conductors because of space weather phenomena. Example GICs are those flowing in power transmission lines via grounded transformer neutrals. Prediction models, used to foresee the amplitudes and waveforms of those currents and to identify weak points in those utilities, depend on the power grid parameters and on the ground resistivity. The differential magnetometer method (DMM), based on dual magnetic measurements, one under a power line and the other at a reference location a few hundred meters away, is used to locally validate those models by indirectly measuring the GIC. We first update our validation results at our DMM stations in Spain using the Earth Resistivity Model of the Iberian Lithosphere and discuss its performance. Second, we propose the use of geomagnetic interstation transfer functions to reproduce the magnetic measurements at the DMM reference location from geomagnetic observatory data, thus reducing the number of field instruments and saving on its maintenance.

Plain Language Summary Space Weather refers to phenomena occurring in the Sun that alter technological systems in and around Earth. We deal with impacts on power grids, where geomagnetically induced currents (GICs) enter the network and can cause problems, for example, damage to power transformers. Models considering the network characteristics and the earth's electrical resistivity help identify weak points of the grid and require validation with real GIC measurements. This can be achieved with the Differential Magnetometer Method, which is based on the difference between the records of two magnetometers: one under the power line and another at a reference location where the GIC effects are negligible. In this paper, the validation is carried out for modeled GIC data obtained by use of the Earth Resistivity Model of the Iberian Lithosphere. We also present a method that uses geomagnetic interstation transfer functions to estimate the reference magnetometer measurements using data from a nearby geomagnetic observatory, thus eliminating the need for the reference measurement.

1. Introduction

Geomagnetically induced currents (GICs) are quasi-direct currents flowing in long terrestrial conductors that ultimately result from a series of complex processes on the Sun. These processes are associated with the emission of large amounts of matter and energy into the interplanetary medium. The main solar phenomena involved are coronal mass ejections, which, by releasing large amounts of magnetized plasma, can significantly increase the density and velocity of the solar wind. When these particles interact with the Earth's magnetosphere and ionosphere, they can cause geomagnetic storms and substorms. At auroral latitudes, the electric fields generated during substorms because of magnetosphere-ionosphere interaction, together with the increase in ionospheric conductivity, lead to an increase in the magnitude of the electrojet currents, which can be in the order of a million amps. As these currents vary with time, an electromagnetic field is generated that propagates down to the Earth's surface, where it is partially reflected and superposed with the incident wave. In the presence of long ground conductors such as power lines, pipelines or even railways, the (geo)electric field of the resulting wave generates the GICs (e.g., Boteler, 1994; Boteler & Pirjola, 2017; Pirjola et al., 2005). However, it should be noted that at low and middle latitudes, as is the case of Spain, it is mainly the currents flowing in the magnetosphere that generate

Project administration: S. Marsal, J. M. Torta, A. Martí, A. Marcuello
Resources: S. Marsal, J. M. Torta, A. Martí, P. Piña-Varas, J. J. Curto, O. Cid, M. Ibañez
Software: S. Marsal, J. M. Torta, A. Martí, P. Piña-Varas, A. Marcuello, J. Ledo, O. Cid
Supervision: S. Marsal, J. M. Torta
Validation: S. Marsal, J. M. Torta, A. Marcuello
Visualization: S. Marsal, J. M. Torta
Writing – original draft: S. Marsal, J. M. Torta
Writing – review & editing: S. Marsal, J. M. Torta, A. Martí, A. Marcuello, J. J. Curto, P. Queralt

the electromagnetic fields responsible for the GIC events (e.g., Torta et al., 2012). Flowing in power grids, GICs can cause problems for utilities, such as reactive power losses, overheating of transformers or malfunctioning of protection relays. In extreme cases, they can lead to power outages due to the failure of such elements, which are otherwise difficult to replace (e.g., Hapgood, 2019).

Given the enormous social and economic impact of such events, more than a decade ago it was considered appropriate to initiate studies to analyze the vulnerability of the Spanish power grid to this phenomenon (Torta et al., 2014). In that initial stage of our modeling, we only considered the 400 kV voltage level and a homogeneous Earth resistivity. After building a model to define the 3D structure of the Earth's resistivity in the Iberian lithosphere, in Torta et al. (2021) we analyzed how the geoelectric field generated by this structure interacts with the power transmission grid by adding also the 220 kV voltage, producing estimates of the expected GIC impacts with new and more accurate vulnerability maps. The assessment was carried out down to the level of the individual windings of each transformer, and examples of the estimated GIC flow were given for substations with numerous power transmission lines converging at diverse orientations. The need to account for lower voltages led us to propose a method to systematically construct an equivalent network and a new method for GIC calculation, that we designated Bus Admittance Matrix (BAM) (Marsal et al., 2022). This technique effectively solves for the current flowing between the buses and the substation neutral point, rather than the Lehtinen and Pirjola (1985) method that solves for the earthing currents at each node, or the Nodal Admittance Matrix that solves for the nodal voltages. BAM will be used in this study to model the GIC flowing in the power lines of the grid from the geoelectric field.

Once the GIC has been estimated, we need to validate it experimentally to assess the reliability of our models. In an initial stage, a system based on Hall effect transducers was deployed to directly monitor the GICs at the neutral of a particular transformer. The 1-kHz sampling frequency of the measurement system, which is still in operation, not only captures the GIC but also detects the 50 Hz current in the neutral caused by power grid or transformer imbalances. If 50 Hz half-cycle saturation is present, it can analyze spectral information up to the tenth harmonic. This helps to determine the transformer's core saturation level due to GIC and can prevent potential thermal damage. However, given the difficulty of such measurements, which involve intrusion into the transformer infrastructure at power grid substations or at power plants, we preferred to carry out the model validations by measuring indirectly and non-invasively through the so-called differential magnetometer method (DMM) in power lines. This technique, based on Ampère's law, determines the intensity of the GIC by measuring its magnetic effects with magnetometers under the lines. Since the magnetic variations recorded continuously by a magnetometer under the line mix the signal of the GIC with that of other natural magnetic phenomena, it is necessary to install a second magnetometer that records the same natural variations, so that the subtraction of both recordings allows obtaining the GIC magnetic signal. For these reasons, this second magnetometer, usually known as the reference magnetometer, should be located far enough away from the line not to record the GIC signal, but close enough to pick up the same ambient magnetic field. Thus, the distance between the two is typically between several hundred meters and a few kilometers. The two facilities are twins, containing the same instrumentation. Although with different variants, this method has recently been used in Brazil (Trivedi et al., 2007), in South Africa and Namibia (Matandirotya et al., 2016), in the UK (Hübert et al., 2020, 2024), and in Canada (Parry et al., 2024); however, we preferred to develop our own equipment and approach. For this purpose, a set of LEMI-44 magnetometers was purchased, which were specifically designed by the manufacturer to meet our requirements. A description of our DMM installations, together with all of our experiences and recommendations on the use of this technique were published in Marsal et al. (2021).

Having progressively deployed a network of DMM measurement stations under various lines of the Spanish power grid and after 4 years analyzing the data obtained from them, in Section 2 we will first describe the DMM network and demonstrate the convenience of its data for the validation of our models. An important lesson learned after these years has been that the deployment of these pairs of stations in optimal working conditions and autonomy in the field entails considerable logistical complexity and the need for frequent travel to these remote sites for the necessary maintenance. This, added to the fact that the number of field instruments is limited, led us to consider the possibility of approaching the design of appropriate transfer functions (TF) so that, taking advantage of the data already recorded at the DMM stations and the continuous records at nearby geomagnetic observatories, we could partially stop recording at these remote sites and still be able to estimate the GICs at those power lines in the future. Our own method to obtain such TFs, based on B-splines, is described in Section 3. Thus, our objective is to infer the DMM reference magnetometer data using the records from the nearest ground magnetometer -

preferably a geomagnetic observatory for quality and continuity reasons. Given the difference of the recorded fields at these two sites, which depends among other factors on their relative distance, this is achieved by means of interstation transfer functions (ITF). Section 4 concludes with a summary and some final remarks. Besides showing more examples of magnetic field inference with ITFs, in Supporting Information S1 we give further details of our method to compute TFs; we show alternative applications of TFs, including inference of the GIC and the computation of the impedance tensor relating magnetic and electric fields; and we compare our method for obtaining the TF with the robust method of Chave and Thomson (2004).

2. Network of DMM Stations and Up-to-Date Validation Results

Details on the instrumentation and deployment of the Spanish temporary DMM network are given in Marsal et al. (2021); we outline here the most important points: LEMI-44 magnetometers are built in PVC cylinders of about 12 cm in diameter and 50 cm in length. To install them in the field, we house them in larger PVC buried cylinders, about 26 cm in diameter and 85 cm high, which, for the correct leveling and orientation, include a concrete base to provide stability, with specially made PVC leveling footscrews accessible from the top. The time signal is provided by a GPS receiver with an external antenna. External connections are made through an appropriate siphon tubing to prevent the entry of rainwater. All external wiring is kept protected against rodents by placing it inside irrigation pipes. Power is supplied by a 12 V, 100 Ah battery. To ensure a certain degree of autonomy, a solar panel is installed with its own battery charger and regulator. The data is stored locally on a Secure Digital card. In addition, the system is equipped with transmission equipment that ensures data retrieval beyond local storage and allows continuous monitoring and immediate diagnosis of possible problems affecting the remote deployments, thus avoiding data loss. The transmission system is low cost and low power and uses a Raspberry Single Board Computer with a General Packet Radio Service connection to transmit the magnetometer data to the Ebre Observatory headquarters once a day.

We have gradually installed the described equipment in temporary stations located under various power lines throughout the Spanish power grid (see map in Figure 1). This deployment aims to derive the GIC where the power grid model, along with the estimated surface impedance, requires validation, often at sites flagged as hazardous due to network topology and resistances.

To derive the GIC from DMM data, we essentially rotate the measured horizontal differences according to the directions parallel and perpendicular to the power line. We then apply Ampère's law, accounting for the distance between wires, their arrangement, and the height of the wires above the magnetometer located below the line (Marsal et al., 2021).

On the other hand, to obtain the modeled GIC, the horizontal geomagnetic field variations were convolved with the surface impedance tensor given by the 3D Electrical Resistivity Model of the Iberian Lithosphere (ERMIL, v1.0) described in Torta et al. (2021) and Ledo et al. (2021). This convolution gave the horizontal geoelectric field, which, integrated along the power lines, provided the required line voltages. From these, the GICs were ultimately calculated using the power grid resistances and characteristics using the BAM method (Marsal et al., 2022). The above procedure is referred to as the standard modeling framework. A new version of the ERMIL model is still in progress, waiting to complete the western part of the Iberian Peninsula with new magnetotelluric (MT) data. In this paper, we consider the former version, since the studied locations are in the eastern part.

To show the utility of the network of DMM stations for model validation purposes, here we will assess the agreement between the derived and the modeled GIC at each DMM station for the events marked in Figure 2. Note that the event selection is based on the horizontal geoelectric field at the most vulnerable substation of the Spanish grid (34 km away from EBR observatory), according to the results of Torta et al. (2021). To evaluate the fit between the modeled and measured GIC time series we will use standard metrics, namely the linear correlation coefficient, ρ, and the performance parameter, P', described in Marsal and Torta (2019). Figure 3 shows graphical examples during the major geomagnetic storm on May 10–12, 2024, with the corresponding values of these metrics. More examples can be found in Marsal et al. (2021) for storm periods in 2021, along with a discussion of the uncertainties inherent to the measurement of the GIC with the DMM method.

Estimates of the geoelectric field assume that the geomagnetic field is uniform across the region and equal to that of the Ebre observatory (EBR). Globally speaking, and in general terms, a more realistic approach would be

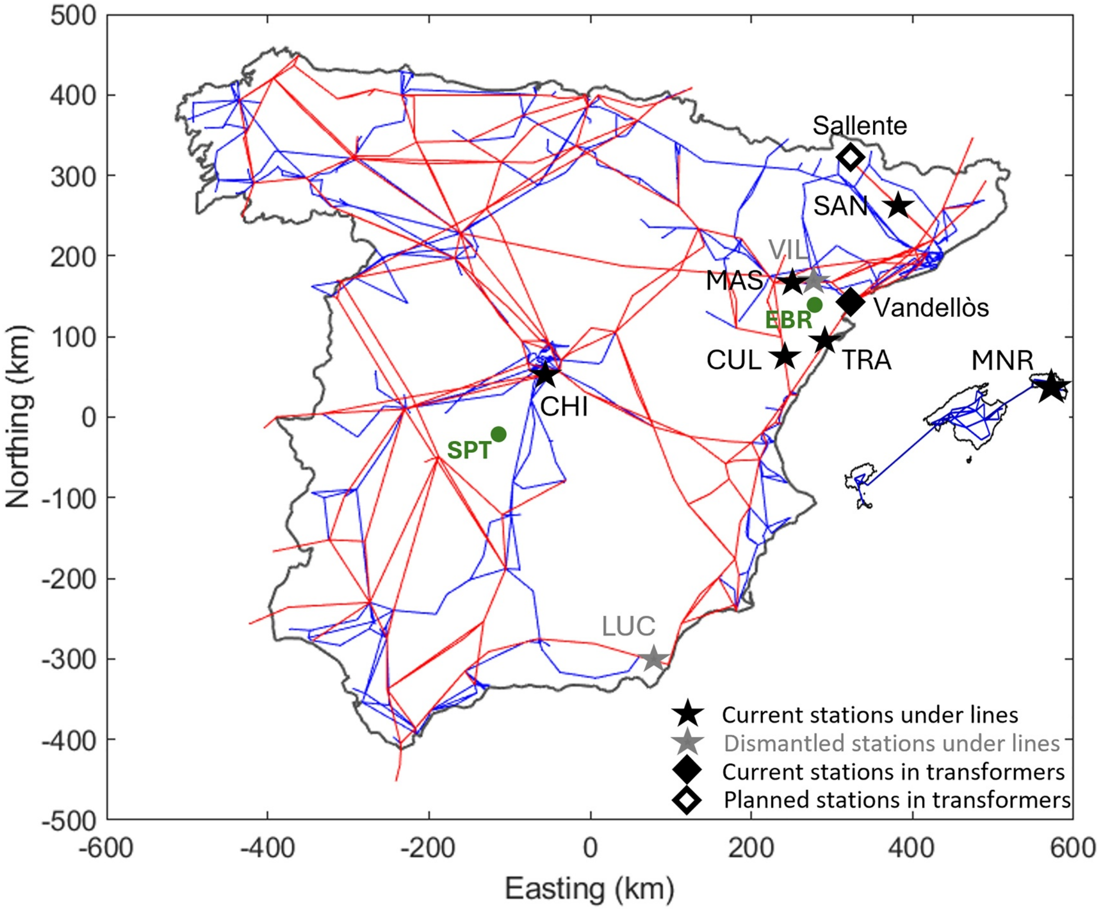

Figure 1. Map of mainland Spain and Balearic Islands showing their power transmission grids. Red and blue lines represent 400 and 220 kV lines, respectively (although voltages are lower in the islands). Symbols indicate either current or dismantled differential magnetometer method stations, as well as current or planned geomagnetically induced current meter on transformers. The three-letter codes assigned refer to the municipality or island where each station is located. EBR and SPT indicate the location of Ebre and San Pablo-Toledo geomagnetic observatories, respectively.

obtained using the Spherical Elementary Current Systems (SECS) method (e.g., Amm & Viljanen, 1999; Marsal et al., 2017; McLay & Beggan, 2010) to interpolate for the geomagnetic variations across the power grid using data from neighboring observatories. However, at midlatitude regions the source fields are fairly uniform, and our experience tells us that the errors made by this simplification are minimal for most sites. In fact, the results obtained from SECS interpolation in Spain do not always outperform those obtained from other interpolation techniques, or simply by choosing the nearest geomagnetic observatory (see Torta et al., 2017), which happens to be EBR for most of the DMM stations, as shown in Figure 1 (see also the discussion on SECS interpolation in Section 3 below and in Text S2.1 of the Supporting Information S1). The GIC flowing in the transmission lines where the DMM stations are located depends on the electric field in and around these stations. This electric field in turn depends on the magnetic field variations, which are well represented by EBR due to its proximity.

Figure 4 shows the metrics assessing the agreement between modeled and measured GIC for the events shown in Figure 2 at each of our DMM stations (the time window analyzed ranges from one to several days, depending on the characteristics of each event). Taking advantage of the fact that CUL started when VIL was already dismantled, and that CHI data started after LUC data deteriorated, we have placed their results in the same graphs (lower panels of Figure 4), respectively.

The parameter ρ $(-1 \leq \rho \leq 1)$ reflects the match between the waveforms of the two signals and is typically close to 1 when the resistivity model being used is a realistic representation of the three-dimensional electrical structure of the underlying lithosphere, although insensitive to changes in scale or biases. In contrast, P' (≤ 1) is more sensitive to the match between the signal amplitudes. Values of P' far from unity or negative could be due to unrealistic

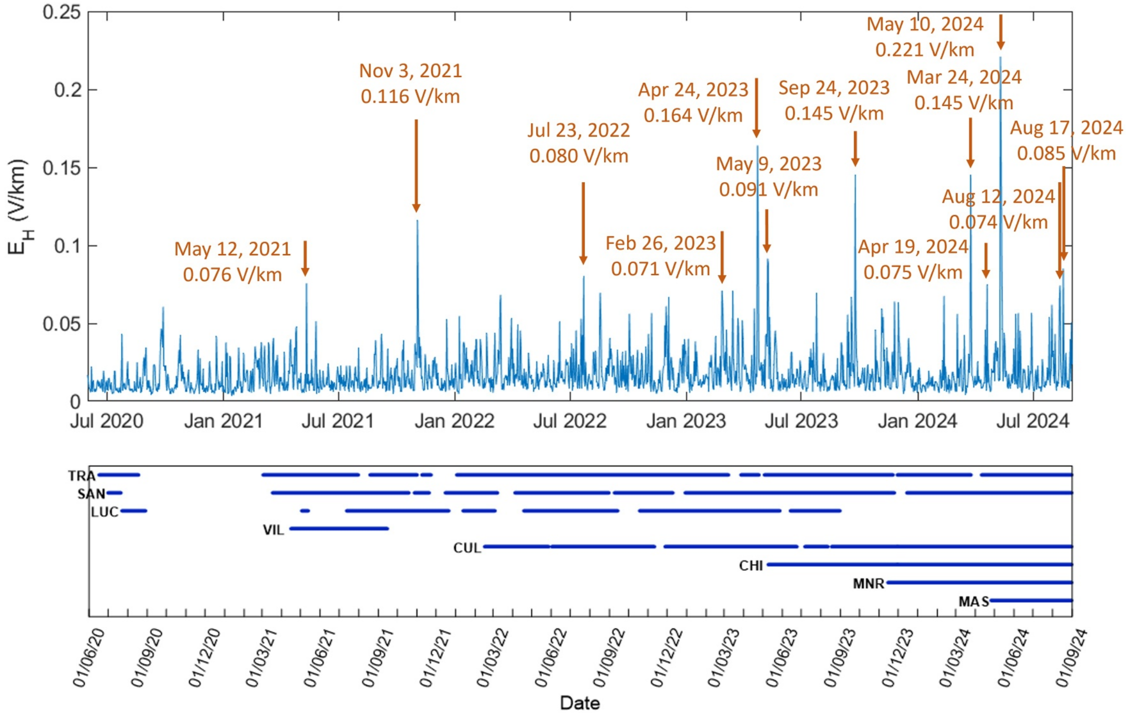

Figure 2. Geomagnetic activity for each day (top) given by the maximum amplitude of the geoelectric field vector at the most vulnerable substation of the Spanish grid. Labeled data tips at the top panel indicate days with data availability at any of the differential magnetometer method stations (bottom) when E_H was equal to or greater than 0.07 V/km.

values of both the impedance tensor elements and the resistances and network topology adopted for modeling the power network. Note that, since these network characteristics (especially transformer winding and grounding resistances) are not always known everywhere, many of them had to be taken from nominal values. For this reason, and because the network voltage levels below 220 kV were ignored, the values of ρ in Figure 4 reflect a better fit than those of P' at all measurement stations. However, P' does not distinguish between underestimation and overestimation. To account for this, similar to Hübert et al. (2024), we performed linear fits between DMM-derived and modeled GICs for selected geomagnetic storms at each site, and looked at the value taken by the slope of that linear function, namely $\mathrm{GIC}_m - \mathrm{GIC}_{\mathrm{DMM}} = p_1\mathrm{GIC}_{\mathrm{DMM}} + p_2$, where GIC_m is the modeled GIC and GIC_{DMM} is the DMM-derived GIC. Positive values of p_1 (also shown in Figure 4) indicate that the model overestimates the amplitude, while negative values show underestimation. However, the time windows chosen to analyze each event include quiet periods, in which noise often masks the signal at some measurement locations, so part of the misfit of the model with respect to the DMM-derived GIC may be due to this fact. It is also the case that the model's response overestimates or underestimates the signal depending on the dominant frequencies of the input signal during different time windows.

Note that the P' and ρ metrics are normalized, and thus do not provide estimates of the typical error in the modeled GIC, ΔGIC, in its physical units (amperes). If, nevertheless, a value is to be given, a rough estimate can be obtained from P' when ρ is close to 1, which is often a reasonable approximation. In this case, it can be shown that $\Delta\mathrm{GIC} \equiv |\mathrm{GIC}_m - \mathrm{GIC}_{\mathrm{DMM}}| \cong (1 - P')|\mathrm{GIC}_{\mathrm{DMM}}|$ (the bars indicate the absolute value). An alternative estimate can be obtained from p_1 if one assumes that $p_2 = 0$, in which case $\Delta\mathrm{GIC} \cong |p_1\mathrm{GIC}_{\mathrm{DMM}}|$, although noisy signals can greatly distort these relationships. Table 1 shows an example of these error estimates for the different DMM stations available during the disturbed period 10–12 May 2024 (see Figure 3).

The ERMIL model provides satisfactory GIC waveform matches (given by ρ); however, the GIC amplitude matches (given by P' and p_1) need to be improved for most events and stations, especially at SAN, CUL and for the only event reported at VIL.

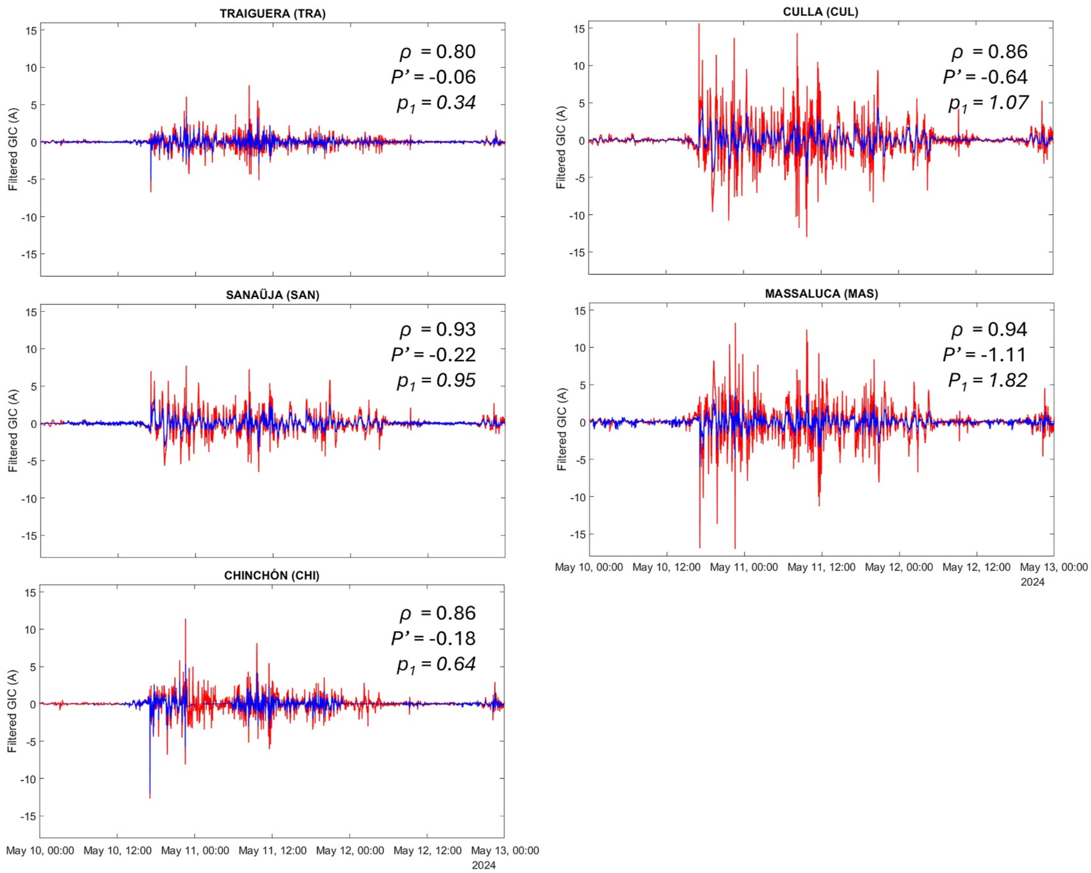

Figure 3. Modeled (red) and measured (blue) geomagnetically induced current at the differential magnetometer method stations available during the May 10–12, 2024 geomagnetic storm, together with the metrics used to assess the fit between the two series.

If we look at the p_1 values, the model significantly overestimates the GIC amplitude at SAN, VIL and CHI (although here the overestimation decreases drastically for the events of August 2024 for some unknown reason). While generally less significant, this also tends to occur at TRA, yet this pattern is occasionally reversed. However, at LUC the GIC signal was always underestimated by the model. Discrepancies observed in some specific events with respect to the regular behavior may be due to the presence of occasional quasi-DC currents not related to GIC in the power line or, more likely, to the transient switching-off of a line or transformer in its vicinity not considered by the network model.

So far, in the Balearic Islands' grid (see Figure 1) we have only captured two significant events, namely those corresponding to 23–25 March and 10–12 May 2024, although unfortunately for the latter, the records corresponding to the most prominent part of the storm are useless due to both instrumental and anthropogenic noise. The model for the Balearic Islands described in Torta et al. (2023) is only able to reproduce the DMM-derived GIC at MNR for these events with $\rho = 0.72$, $P' = -1.21$, $p_1 = 1.044$, and $\rho = 0.84$, $P' = -1.07$, $p_1 = 1.369$, respectively. This mismatch is not surprising since (a) the expected GIC amplitudes are very low because of the small size of the Balearic grid and because the voltage levels used are lower than those of mainland Spain (conductors used at lower voltage levels tend to be of higher resistance); (b) the information collected on grid resistance values was scarce and mostly nominal values had to be used; (c) the lithospheric resistivity model used is predictably less accurate than the ERMIL, as it was not derived from an inversion of empirical MT data, but simply relied on crustal and lithospheric information, and only used resistivity values from MT data on the island of Mallorca as a constraint; and (d) the reference DMM station was installed in a very noisy location within a busy cow farm with a mobile irrigation system in the vicinity.

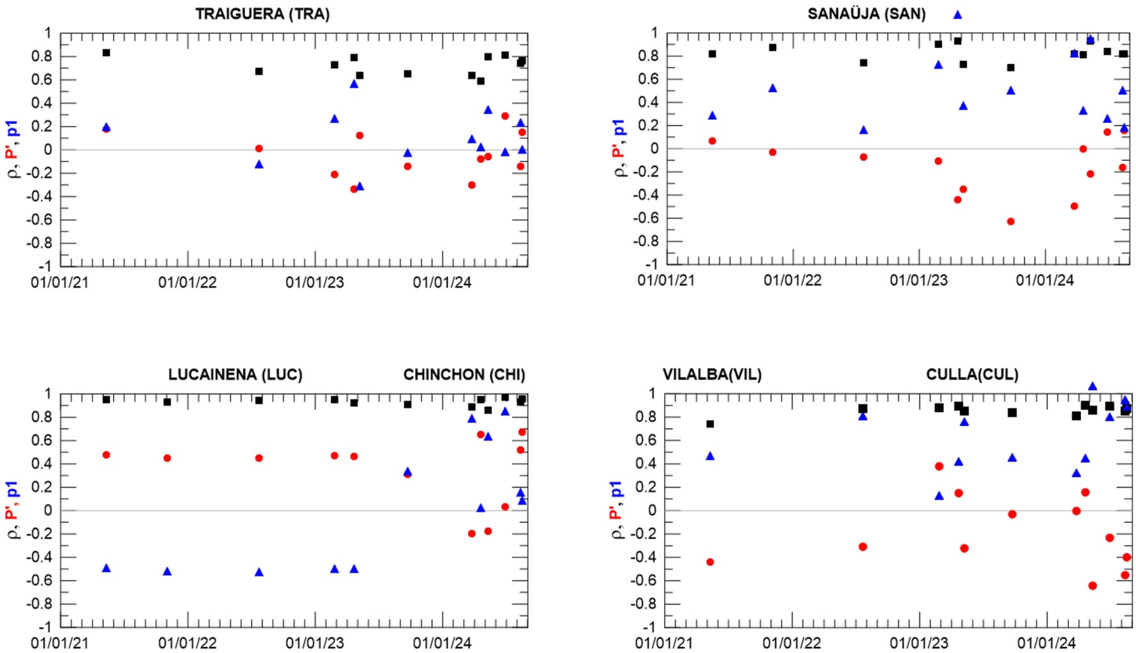

Figure 4. Linear correlation coefficient (ρ—black squares), performance parameter (P'—red circles) and slope of the linear fit (p_1—blue triangles) to evaluate the agreement between DMM-derived and modeled geomagnetically induced current at Traiguera (TRA, top left), Sanaüja (SAN, top right), Lucainena (LUC) and Chinchón (CHI, bottom left), and Vilalba (VIL) and Culla (CUL, bottom right) stations with available data during the events indicated in Figure 2 until the end of August 2024. Values of the parameters ρ, P' and $p1$ close to 1, 1, and 0 resp. indicate a good match.

The case of La Pobla de Massaluca (MAS), under one of the power lines identified as the most hazardous according to our modeling results (Torta et al., 2021), deserves special attention. In 2021 we had already maintained a DMM station under that line in Vilalba (VIL), but we dismantled it after a few months of operation (see Figures 1 and 2) because its data contained too much noise. In Marsal et al. (2021) we pointed out the possibility that this was due to signals or their harmonics circulating on the line itself due to power grid switching or voltage transients caused by high power demands. Another possible reason for such disturbances could be related to the existence of wind turbines in the vicinity of the power line path, or due to stray currents in a nearby pylon. At the end of May 2024, we decided to redeploy the magnetometers a few kilometers away, in the hope of improving the signal-to-noise ratio of the recordings. Despite only measuring for 4 months, the fact that we are reaching the solar cycle maximum allowed us to analyze the behavior of its data for several events (see Figure 5).

Analyzing the geomagnetic time series recorded at MAS and the GICs derived from them (see Text S1 in the Supporting Information S1) we realize that, unfortunately, the noise detected 3 years earlier at VIL persists, and it significantly masks the GIC signal during minor geomagnetic storms (e.g., 16/05/2024 and 07/06/2024), providing poor correlations and performance parameters when comparing the DMM-derived and modeled GICs.

Table 1
Error (in Amps) in the Modeled Geomagnetically Induced Current for the Disturbed Period 10–12 May 2024

	RMS ΔGIC	RMS $\Delta\mathrm{GIC}_{P'}$	RMS $\Delta\mathrm{GIC}_{p1}$	Max ΔGIC	Max $\Delta\mathrm{GIC}_{P'}$	Max $\Delta\mathrm{GIC}_{p1}$
TRA	0.42	0.42	0.14	5.13	5.51	1.80
SAN	0.72	0.67	0.52	5.10	4.26	3.31
CHI	0.68	0.63	0.34	6.39	14.15	7.66
CUL	1.52	1.41	0.91	12.89	8.11	5.27
MAS	1.46	1.34	1.16	11.61	12.57	10.90

Note. The error is evaluated in different ways, either directly subtracting modeled and observed series (ΔGIC), or with approximations based on P' ($\Delta\mathrm{GIC}_{P'} \equiv (1 - P')|\mathrm{GIC}_{\mathrm{DMM}}|$) or p_1 ($\Delta\mathrm{GIC}_{p1} \equiv |p_1\mathrm{GIC}_{\mathrm{DMM}}|$).

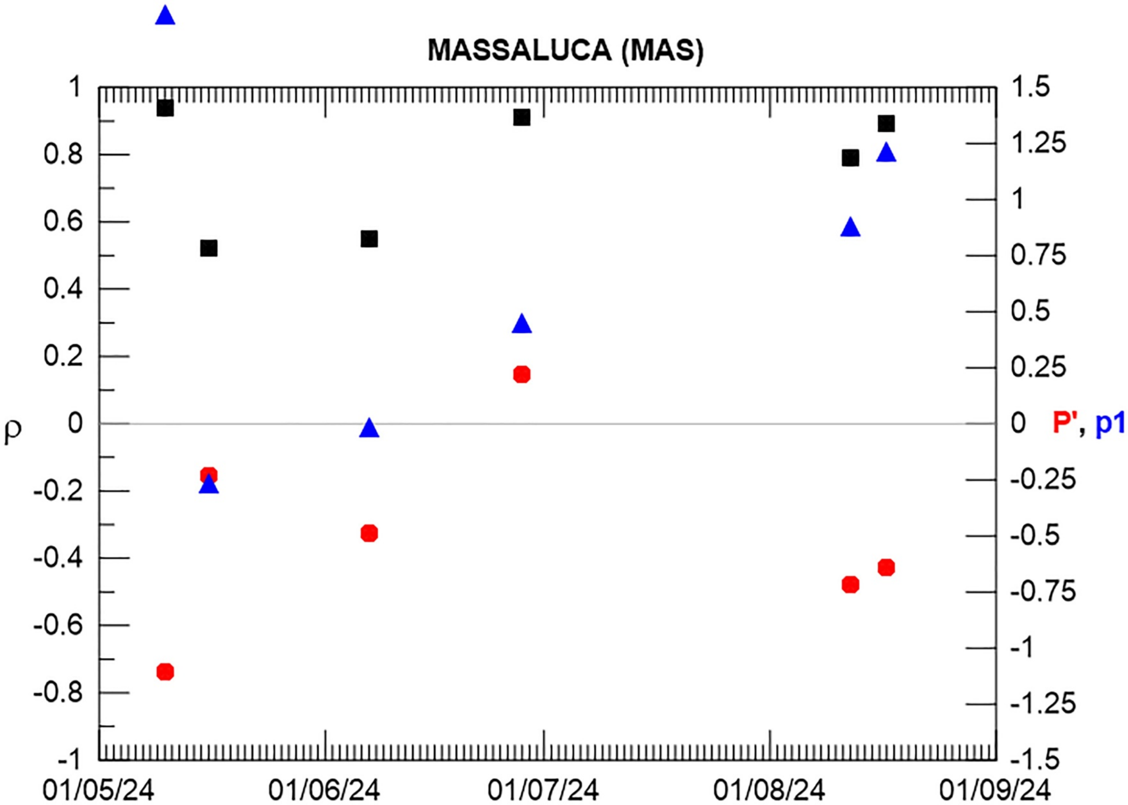

Figure 5. Same as Figure 4 for La Pobla de Massaluca (MAS) station. Note that we have added three extra events with respect to those shown in Figure 2, corresponding to minor or moderate geomagnetic storms (16/05/2024, 07/06/2024, and 28/06/2024).

Since the GIC signal was much stronger during the severe geomagnetic storm starting on 10/05/2024, ρ improved markedly. For reasons beyond our control, the noise attenuated very significantly during the moderate storm on 28/06/2024 and, consequently, both metrics improve, with the DMM-derived GIC achieving a good match with the modeled GIC for low frequencies, although the model overestimates the empirical signal at higher frequencies. To date, proper validation of the model in MAS must only be taken from the comparison extracted on the latter event, when the signal prevailed over the noise even in the quiet periods. In addition, the ERMIL model needs to be improved in this area to achieve better parameters P' and ρ. In consequence, as far as MAS station is concerned, the comparison between DMM-derived versus modeled GIC can be misleading during times when the signal-to-noise ratio is low. This restricts our comparison to severe geomagnetic storms, or just to short time intervals during moderate storms, when the signal is clearly above the half-width of approximately 0.5 A of the noise.

3. Inferring the DMM Reference B-Field From Magnetic Observatory Data

We now turn to the subject of TF. Our first objective is to take advantage of available records from nearby, high-quality geomagnetic observatories to emulate the data provided by the reference magnetometer of the DMM station. Success would make it possible to dispense with this magnetometer, thus avoiding data acquisition problems, decreasing the cost of each DMM site, and streamlining site installation logistics.

Consider locations close enough on the Earth's surface to assume that the external sources of the geomagnetic field are the same, although the conductivity of the subsurface may be different. This is justified if the scale length of variations at the source region, or the distance to the source, are much larger than the distance between those locations on the surface (e.g., Boteler & Pirjola, 1998, although the complex image method is only valid for 1-D Earth conductivity and simple line source ionosphere current). Under these conditions, the horizontal projection of the geomagnetic field at one location, say $\vec{B}_T$, can be expressed in terms of that at the other location, $\vec{B}_O$, as

10.1029/2024SW004180

$$\vec{B}_T(f) = \mathbf{H_{TO}}(f)\,\vec{B}_O(f), \tag{1}$$

where $\mathbf{H_{TO}}$ is the frequency-dependent magnetic interstation tensor between sites T and O expressed as a 2×2 matrix (e.g., Berdichevsky & Dmitriev, 2008; Campanya et al., 2014, 2019). $\vec{B}_T$ and $\vec{B}_O$ are given in the frequency domain, and the effect of $\mathbf{H_{TO}}$ on $\vec{B}_O$ is that of a TF to obtain the target field $\vec{B}_T$. Equation 1 derives from the fact that a pure plane wave with vertical incidence and frequency f is reflected by the conducting Earth as a wave with the same frequency though generally different amplitude, phase and polarization, due to the local and nearby conductivity structures in the subsurface. Depending on the dimensionality of these structures, there may be a net transfer of energy from one horizontal component of the geomagnetic field to the other. Thus, for homogeneous and 1-D media, there is no transfer between components and the $\mathbf{H_{TO}}$ tensor is diagonal, whereas for higher dimensionalities the tensor has non-zero off-diagonal components.

Note that the expression of the geomagnetic interstation transfer function (ITF) $\mathbf{H_{TO}}$ is uniquely defined for each pair of sites T and O. In the DMM context, T (the *target*) denotes the reference site, typically located a few hundred meters from the power line, while O refers to the nearest geomagnetic *observatory* - or variometric station in its absence.

Although standard techniques exist within the MT community to obtain $\mathbf{H_{TO}}$ (e.g., Chave & Jones, 2012; Chave & Thomson, 2004), we illustrate here our alternative inversion method, which we have chosen because we successfully tested it in previous work (e.g., Marsal et al., 2020) (a comparison with a standard technique can be found in Text S2.2 of the Supporting Information S1). Let $X_T(f)$ and $Y_T(f)$ be the frequency domain North and East components (obtained, e.g., by use of the Fast Fourier Transform), respectively, of the geomagnetic field at site T, that is, $\vec{B}_T(f) = (X_T(f), Y_T(f))$. Similar definitions apply to site O. Then, Equation 1 can be written explicitly as

$$\begin{pmatrix} X_T \\ Y_T \end{pmatrix} = \begin{pmatrix} H_{11} & H_{12} \\ H_{21} & H_{22} \end{pmatrix} \begin{pmatrix} X_O \\ Y_O \end{pmatrix}, \tag{2}$$

where all the variables are functions of f. To determine the expression of the $\mathbf{H_{TO}}$ elements, write them as a series of cubic B-spline functions b_j in the frequency domain, that is,

$$\begin{array}{ll} H_{11}(f) = \sum_{j=1}^{m} \alpha_j b_j(f); & H_{12}(f) = \sum_{j=1}^{m} \beta_j b_j(f) \\ H_{21}(f) = \sum_{j=1}^{m} \gamma_j b_j(f); & H_{22}(f) = \sum_{j=1}^{m} \delta_j b_j(f) \end{array}. \tag{3}$$

where the weights $\alpha_j, \beta_j, \gamma_j$, and δ_j are the unknowns to be determined. Note that the frequency domain expressions of the horizontal magnetic components X and Y involves complex numbers, which extend to the elements of $\mathbf{H_{TO}}$, and thus to the weights of the B-splines to be determined, since b_j are real (known) functions.

Thus, for the North component at site T, and for each of the n frequencies f_i of the spectrum, we have

$$X_T(f_i) = H_{11}(f_i) X_O(f_i) + H_{12}(f_i) Y_O(f_i) = \sum_{j=1}^{m} \alpha_j b_j(f_i) X_O(f_i) + \sum_{j=1}^{m} \beta_j b_j(f_i) Y_O(f_i), i = 1 \dots n \tag{4}$$

which can be written in matrix form as

$$\begin{pmatrix} X_T(f_1) \\ X_T(f_2) \\ \vdots \\ X_T(f_n) \end{pmatrix} = \begin{pmatrix} X_O(f_1)b_1(f_1)\cdots X_O(f_1)b_m(f_1) & Y_O(f_1)b_1(f_1)\cdots Y_O(f_1)b_m(f_1) \\ X_O(f_2)b_1(f_2)\cdots X_O(f_2)b_m(f_2) & Y_O(f_2)b_1(f_2)\cdots Y_O(f_2)b_m(f_2) \\ \vdots \quad \ddots \quad \vdots & \vdots \quad \ddots \quad \vdots \\ X_O(f_n)b_1(f_n)\cdots X_O(f_n)b_m(f_n) & Y_O(f_n)b_1(f_n)\cdots Y_O(f_n)b_m(f_n) \end{pmatrix} \cdot \begin{pmatrix} \alpha_1 \\ \vdots \\ \alpha_m \\ \beta_1 \\ \vdots \\ \beta_m \end{pmatrix}. \tag{5}$$

Equation 5 is written in compact form as $\mathbf{T} = \mathbf{S} \cdot \boldsymbol{\alpha}$, where $\mathbf{T}$ (the target field) is $(n \times 1)$ in size and $\mathbf{S}$ is $(n \times 2m)$. The relation between the number of spline basis functions, m, and the number of frequencies, n, is chosen so that each basis contains multiple frequencies (typically 64), so the resulting overdetermined system is solved for the $(2m \times 1)$ matrix $\boldsymbol{\alpha}$ by an appropriate inversion algorithm such as (regularized) least squares (RLS) (see Text S3 in the Supporting Information S1 for more details on the algorithm applied). Note that the same expressions (4) and (5) hold for the Y_T component replacing $\{H_{11}, H_{12}\}$ with $\{H_{21}, H_{22}\}$ and $\{\alpha_j, \beta_j\}$ with $\{\gamma_j, \delta_j\}$.

The system of Equation 5 determining the weights is best defined from $\vec{B}_T$ and $\vec{B}_O$ fields corresponding to disturbed conditions, since they provide an improved signal-to-noise ratio at high frequencies. Once these have been determined, the set of Equation 3 allows us to find an expression for the elements of $\mathbf{H_{TO}}$, which should be applicable to obtain $\vec{B}_T$ from $\vec{B}_O$ for any other time interval, provided the sites T and O remain the same.

The use of ITFs to generate effective data for DMM deployments in Spain is effective for distances up to a few hundred kilometers between sites T and O. At locations where the plane wave approximation loses validity, for example at high geomagnetic latitudes and especially under the auroral zone, care should be taken with their use, as the spatial range of effectiveness may be reduced.

Before going on to illustrate the application of the ITF, it seems useful to add some discussion of other methods for geomagnetic data interpolation, of which SECS is perhaps the most popular (e.g., Marsal et al., 2020; McLay & Beggan, 2010; Weygand et al., 2021). Indeed, it is possible to obtain a good representation of the magnetic field variations at a target location within a network of well distributed magnetometers, assuming current sources above (primary fields) and below the Earth's surface (induced fields). Thus, in principle, this technique could be used for the same purposes as those pursued in this section. Although no comprehensive comparison has been made, preliminary tests on the Iberian Peninsula show that SECS interpolation performs worse than ITF inference (see Text S2.1 in the Supporting Information S1). The main reason for this is that without a sufficiently dense magnetometer grid, the role of local/regional subsurface geological structures or nearby sea bodies is poorly taken into account by the SECS method. The ITF, in contrast, implicitly accounts for the different electrical conductivities in the subsurface between the primary observatory and the target locations. Other arguments in favor of the ITF method over SECS are primarily practical: previously available data from multiple observatories must be collected, quality controlled and appropriately processed, often individually and in a way that is difficult to automate. The latter implies several steps, among which adequate treatment of data gaps, which are more likely as the number of observatories involved increases. Finally, the algorithm for SECS requires a matrix inversion for each time step, which slows down the process. The ITF method, in contrast, only requires measured data at the nearest observatory and at the target location, and the transfer function only needs to be determined once. We note, however, that ITFs are likely to be outperformed by SECS at higher latitudes under dense magnetometer networks such as the International Monitor for Auroral Geomagnetic Effects (IMAGE), for two reasons: first, the density of magnetometers allows a suitable application of the latter technique (e.g., Juusola et al., 2015; Pulkkinen et al., 2003), and second, the primary source fields are highly spatially variable during perturbed periods, which undermines the plane wave assumption and thus the use of the ITF.

Figure 6 shows the reconstructed magnetic field at the DMM station of Culla (CUL), acting as the site T, with data from Ebre (EBR) observatory, 81 km away, acting as the site O (see map in Figure 1). The original 1-s data have been band-pass filtered to allow frequencies corresponding to periods between 2 min (to smooth high-frequency undesired signals) and 5 hr (thus avoiding drifts or temperature effects on the magnetometers). In this case, the

10.1029/2024SW004180

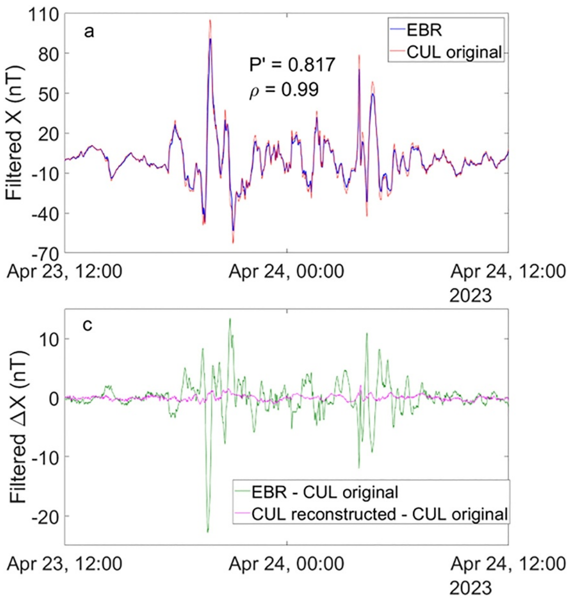

Figure 6. (a) North component variations of the magnetic field at EBR observatory (blue) and at the original (target) differential magnetometer method reference magnetometer of CUL (red) for a magnetically disturbed 1-day period starting at noon on 23 April 2023. (b) The same variations at CUL but reconstructed from EBR data (blue) and the target CUL data again (red). (c) Difference between the signals in panel (a) (green), and difference between signals in panel (b) (magenta).

ITF $\mathbf{H_{TO}}$, determined by inversion of Equation 5 (and the corresponding equation for Y_T) for an event occurred on 5 November 2023 (maximum Kp = 7+), has been applied to the shown event, straddling 23–24 April 2023 (maximum Kp = 8+). The similarity between the target and reconstructed magnetic field variation curves is also evaluated here with the performance parameters P' and ρ, for which values close to unity denote a good match.

Figure 7 shows the reconstructed magnetic East component for the DMM reference station at Chinchón (CHI), 330 km away from EBR. In this case, $\mathbf{H_{TO}}$ has been determined from the same event on 5 November 2023, and has been applied to the October 26–29, 2023, moderately disturbed event (maximum Kp = 5−).

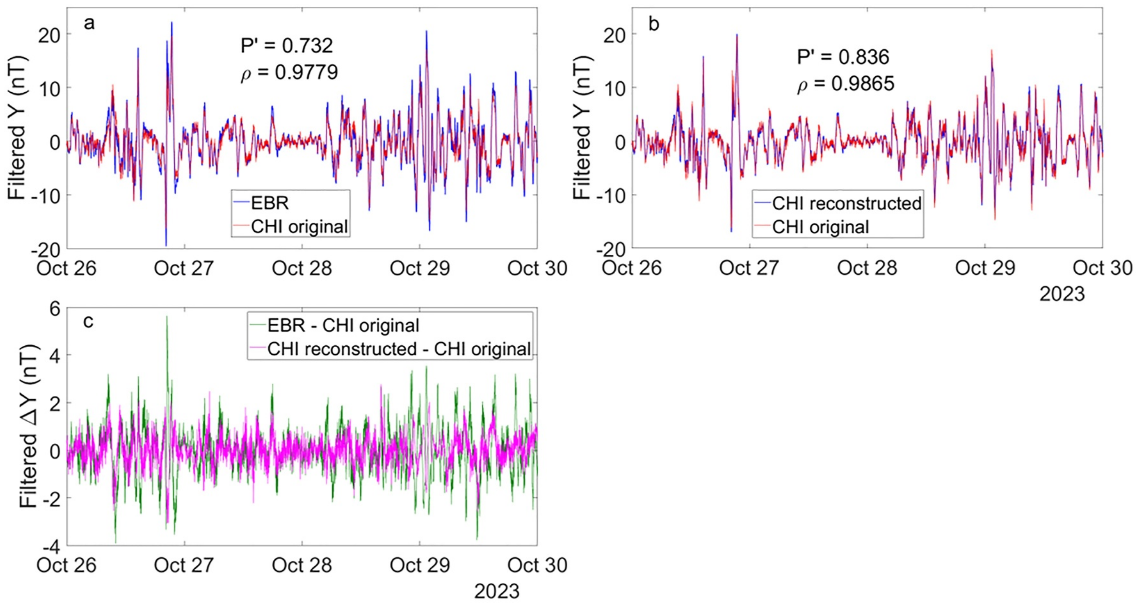

Figure 7. (a) East component variations of the magnetic field at EBR observatory (blue) and at the original (target) differential magnetometer method reference magnetometer of CHI (red) for a magnetically disturbed 4-day period starting on 26 October 2023. (b) The same variations at CHI but reconstructed from EBR data (blue) and the target CHI data again (red). (c) Difference between the signals in panel (a) (green), and difference between signals in panel (b) (magenta).

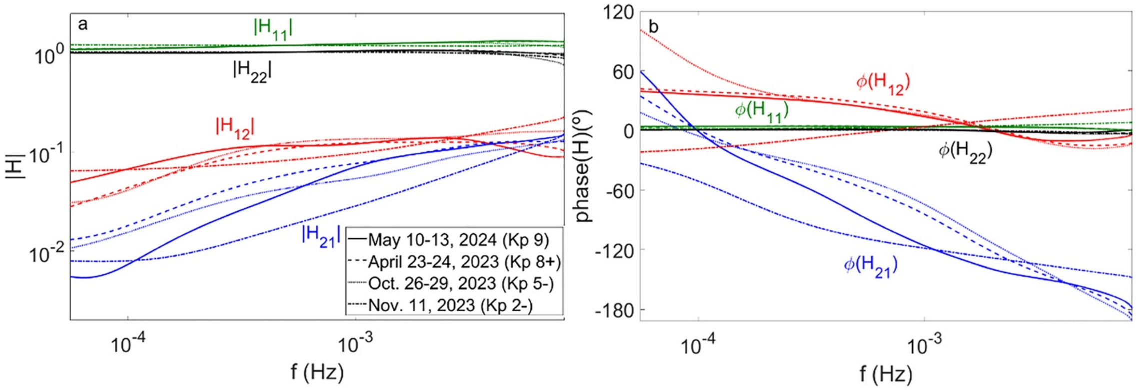

Figure 8. Components of the **H** tensor between EBR observatory and the reference site of CUL differential magnetometer method station as a function of frequency, *f*. Each color (green, red, blue, black) represents a tensor component ($\boldsymbol{H_{11}}, \boldsymbol{H_{12}}, \boldsymbol{H_{21}}, \boldsymbol{H_{22}}$, resp.); the different line styles (solid, dashed, dotted, dot-dash) of the same color represent the tensor components obtained from periods with different degrees of disturbance (May 10–13, 2024; April 23–24, 2023; October 26–29, 2023, 11 November 2023, whose maximum Kp′s are 9, 8+, 5−, 2−, resp.) (a) Complex magnitude (unit-less) and (b) phase, in degrees.

In the figures, P' and ρ are shown both for the original magnetic fields at sites T and O, that is, before the application of the ITF (Figures 6a and 7a), and for the match between the target and the reconstructed magnetic fields, that is, after the application of the ITF (Figures 6b and 7b). Note that the latter gets values closer to unity than the former, denoting the efficiency of the ITF to reproduce the target field. It should be noted that the direct use of EBR data as a proxy for the reference site of the nearest DMM station (CUL) would result in absolute differences of up to 23 nT (Figure 6c, green curve), which would be erroneously attributed to the magnetic effect of the GIC affecting the magnetometer below the transmission line. This difference is typically translated to a few amps in the GIC. With the reconstructed signal, the error is reduced to one tenth in this example (Figure 6c, magenta curve).

On the other hand, the improvement in the reconstructed field is less significant at the reference magnetometer of the furthest DMM station (Figure 7c). In this case, however, data from the closest observatory of San Pablo-Toledo, 105 km away from CHI, provides a better match with the target data, achieving values $P' = 0.90$ and $\rho = 0.995$.

Text S2 in the Supporting Information S1 shows examples of B-field inference for the storm that started on 10 May 2024, which has been classified as "extreme", with Kp values of 9. The examples shown are good evidence for the validity of our method, since one of the ITFs, determined from a moderately disturbed event, can reproduce remarkably well the B-field during the highly perturbed conditions of this major storm.

Although our main purpose of reproducing the target field from geomagnetic observatory data is reasonably well achieved, we dedicate some lines to the transfer function tensor itself, which has been overlooked so far. Figure 8 shows the four components of the interstation tensor **H** between EBR observatory and the reference site of CUL DMM station as a function of frequency, *f*. Specifically, Figures 8a and 8b represent the complex magnitude and the phase of the tensor components, respectively. Each color in the plot represents a tensor component; the different line styles of the same color represent the tensor components obtained from periods with different degrees of disturbance, whose maximum Kp values range from 2- to 9. This serves as a stationarity test, since ideally the results between the same two stations should be independent of the disturbed period from which they were derived.

To start, as expected for nearby stations, **H** is seen to be close to the identity matrix for all frequencies, that is, H_{11} and H_{22} are close to unity (with phase 0°), and much greater than H_{12} and H_{21} (with an arbitrary phase). A closer examination reveals that the curves corresponding to the less disturbed intervals (Kp 5- and especially Kp 2-) tend to be more divergent, which can be explained by the worse determination of the B-spline coefficients due to an increase of noise compared to signal (i.e., a lower signal-to-noise ratio) in the original magnetic time series, especially that of the DMM station. This is clearly seen for the phase of H_{12} (i.e., $\phi(H_{12})$), and to a lesser extent for $\phi(H_{21})$ and $|H_{21}|$ (see the corresponding dotted-dashed lines, for which Kp = 2-).

Transfer functions can also be used for other purposes beyond inference of the DMM reference field. Ingham et al. (2017), for example, used TFs derived with power spectral techniques to predict the GIC flowing in New Zealand transformers from geomagnetic observatory data. Our method based on B-splines provides an alternative means to derive the TF. Text S4 in the Supporting Information S1 provides the mathematical background of this application, along with two examples aimed at predicting the GIC flowing in a transmission line where previous DMM measurements were performed.

Another application of TFs is in the field of magnetotellurics. In this case, it is the TF itself (called the impedance tensor), which relates the co-located measured electric and magnetic fields, that is of interest as it provides information about the conductivity of the subsurface. An attempt to use our technique to compute the impedance tensor is given in the Text S4.2 in Supporting Information S1, together with a discussion on the limitations encountered.

4. Discussion and Conclusions

The DMM method is useful for GIC research because it allows validation of models aimed at identifying vulnerable points on critical human infrastructures consisting of long terrestrial conductors that may be subject to harmful DC currents flowing in the case of severe Space Weather. A clear example of such critical infrastructure is the power grid. These models depend both on a reliable ground resistivity model to calculate the geoelectric field from the available geomagnetic data, and on the appropriate parameters (e.g., resistances and topology) of the power network under study. This makes it challenging to differentiate between these two sources of uncertainty in case of disagreements between DMM measurements and predictions. The use of the P' and ρ performance parameters, however, may provide certain clues. Small ρ (correlation) values, mostly sensitive to the signal waveform, are rarely indicative of inadequate grid parameters, but rather of deficiencies of the resistivity model, although they could be also due to many factors such as source field assumptions, bandlimited signals/impedances, AC effects, etc. Conversely, small P' values rather denote inappropriate grid parameters, but also can indicate inadequate scaling values in the apparent resistivity of the subsurface model.

We have developed TFs providing practical reconstructions of the B-field measured by the DMM reference magnetometer (the one unaffected by the GIC) with data from a nearby geomagnetic observatory (up to a few hundred kilometers in the case of mid-latitude Spain). Thus, provided that previous DMM measurements have been made near a power transmission line, our suggested procedure offers the possibility to dispense with the use of the reference magnetometer once the appropriate ITFs have been determined. Our experience shows that moderately disturbed conditions (e.g., Kp = 5-) are sufficient to obtain effective ITFs capable of reproducing the magnetic variations of extreme storms (see Text S2.1 in the Supporting Information S1).

TFs have also been applied with reasonable success to infer the GIC from observatory B-field data (see Text S4.1 in the Supporting Information S1), so it is even possible to dispense with the line magnetometer and, from the records of a relatively nearby geomagnetic observatory, still obtain fairly accurate estimates of the GIC flowing in that line provided that the network has not changed. This may have applications in predicting extreme event scenarios (Ingham et al., 2017). Alternatively, since the TF method provides an estimate of line GIC for a single fixed (unknown) network configuration anchored to a fixed point in time, comparison of the TF estimate with subsequent DMM measurements can help to identify changes in network state over time, which is key to the standard modeling framework. Finally, in the Text S4.2 in Supporting Information S1 we have examined the reliability of the method to obtain TFs by comparing the output with a known input applied to the impedance tensor relating local B and E-fields. The results are good for most of the frequency spectrum, although with differences at the ends (high and low frequencies) due to limitations of our procedure.

Data Availability Statement

The geomagnetic observatory data were obtained from www.intermagnet.org. In addition, EBR geomagnetic data are available from https://www.obsebre.es/en/magnetismdatacatalogs/en-om-data-catalogs-ebre. The magnetometer data to derive the GIC are available in this in-text data citation reference: Marsal et al. (2024) (under license CC-BY-ND).

Acknowledgments

This research has been supported by Spanish projects PID2020-113135RB-C32 and PID2020-113135RB-C31 funded by Ministerio de Ciencia e Innovación. We are grateful to the owners of the lands where we have deployed our instruments for lending us a space free of charge. Some of the results presented in this paper rely on data collected at geomagnetic observatories; we thank the national institutes that support them, and INTERMAGNET for promoting high standards of geomagnetic observatory practice.

References

Amm, O., & Viljanen, A. (1999). Ionospheric disturbance magnetic field continuation from the ground to the ionosphere using spherical elementary current systems. *Earth Planets and Space*, *51*(6), 431–440. https://doi.org/10.1186/BF03352247

Berdichevsky, M. N., & Dmitriev, V. I. (2008). *Models and methods of magnetotellurics*. Springer-Verlag. https://doi.org/10.1007/978-3-540-77814-1

Boteler, D. (2014). Methodology for simulation of geomagnetically induced currents in power systems. *Journal of Space Weather and Space Climate*, *4*, A21. https://doi.org/10.1051/swsc/2014018

Boteler, D. H. (1994). Geomagnetically induced currents: Present knowledge and future research. *IEEE Transactions on Power Delivery*, *9*(1), 50–58. https://doi.org/10.1109/61.277679

Boteler, D. H., & Pirjola, R. J. (1998). The complex-image method for calculating the magnetic and electric fields produced at the surface of the Earth by the auroral electrojet: The complex-image method. *Geophysical Journal International*, *132*(1), 31–40. https://doi.org/10.1046/j.1365-246x.1998.00388.x

Boteler, D. H., & Pirjola, R. J. (2017). Modeling geomagnetically induced currents. *Space Weather*, *15*(1), 258–276. https://doi.org/10.1002/2016SW001499

Campanyà, J., Gallagher, P. T., Blake, S. P., Gibbs, M., Jackson, D., Beggan, C. D., et al. (2019). Modeling geoelectric fields in Ireland and the UK for space weather applications. *Space Weather*, *17*(2), 216–237. https://doi.org/10.1029/2018SW001999

Campanya, J., Ledo, J., Queralt, P., Marcuello, A., & Jones, A. G. (2014). A new methodology to estimate magnetotelluric (MT) tensor relationships: Estimation of Local transfer-functions by Combining Interstation Transfer-functions (ELICIT). *Geophysical Journal International*, *198*(1), 484–494. https://doi.org/10.1093/gji/ggu147

Chave, A. D., & Jones, A. G. (2012). *The magnetotelluric method*. Cambridge University Press. https://doi.org/10.1017/CBO9781139020138

Chave, A. D., & Thomson, D. J. (2004). Bounded influence magnetotelluric response function estimation. *Geophysical Journal International*, *157*(3), 988–1006. https://doi.org/10.1111/j.1365-246X.2004.02203.x

Hapgood, M. (2019). Technological impacts of space weather. In *Geomagnetism, aeronomy and space weather: A journey from the Earth* (pp. 251–264). s Core to the Sun. https://doi.org/10.1017/9781108290135.017

Hübert, J., Beggan, C. D., Richardson, G. S., Gomez-Perez, N., Collins, A., & Thomson, A. W. P. (2024). Validating a UK geomagnetically induced current model using differential magnetometer measurements. *Space Weather*, *22*(2). https://doi.org/10.1029/2023SW003769

Hübert, J., Beggan, C. D., Richardson, G. S., Martyn, T., & Thomson, A. W. P. (2020). Differential magnetometer measurements of geomagnetically induced currents in a complex high voltage network. *Space Weather*, *18*(4), e2019SW002421. https://doi.org/10.1029/2019SW002421

Ingham, M., Rodger, C. J., Divett, T., Dalzell, M., & Petersen, T. (2017). Assessment of GIC based on transfer function analysis. *Space Weather*, *15*(12), 1615–1627. https://doi.org/10.1002/2017SW001707

Juusola, L., Viljanen, A., van de Kamp, M., Tanskanen, E. I., Vanhamäki, H., Partamies, N., & Kauristie, K. (2015). High-latitude ionospheric equivalent currents during strong space storms: Regional perspective. *Space Weather*, *13*(1), 49–60. https://doi.org/10.1002/2014SW001139

Ledo Fernández, J., Piña-Varas, P., Queralt i Capdevila, P., Martí i Castells, A., & Marcuello Pascual, A. (2021). Magnetotelluric impedances to build the Electrical Resistivity Model of Iberian Lithosphere (ERMIL1.0). *CORA. Repositori de Dades de Recerca*, V1. https://doi.org/10.34810/data120

Lehtinen, M., & Pirjola, R. J. (1985). Currents produced in earthed conductor networks by geomagnetically-induced electric fields. *Annales Geophysicae*, *3*(4), 479–484.

Liu, M. Z., Xie, Y. Z., Yang, Y. F., Trinchero, R., & Stievano, I. S. (2023). Reduced nodal admittance matrix method for probabilistic GIC analysis in power grids. *IEEE Transactions on Power Systems*, *38*(5), 4950–4953. https://doi.org/10.1109/TPWRS.2023.3280392

Marsal, S., & Torta, J. M. (2019). Quantifying the performance of geomagnetically induced current models. *Space Weather*, *17*(7), 941–949. https://doi.org/10.1029/2019sw002208

Marsal, S., Torta, J. M., Canillas-Pérez, V., & Curto, J. J. (2022). A new standalone tool for DC-equivalent network generation and GIC calculation in power grids with multiple voltage levels. *Space Weather*, *20*(3). https://doi.org/10.1029/2021sw002984

Marsal, S., Torta, J. M., Curto, J. J., Canillas-Pérez, V., Cid, O., Ibañez, M., & Marcuello, A. (2021). Validating GIC modeling in the Spanish power grid by differential magnetometry. *Space Weather*, *19*(12), 1–17. https://doi.org/10.1029/2021SW002905

Marsal, S., Torta, J. M., Pavón-Carrasco, F. J., Blake, S. P., & Piersanti, M. (2020). Including the temporal dimension in the SECS technique. *Space Weather*, *18*(10). https://doi.org/10.1029/2020SW002491

Marsal, S., Torta, J. M., Segarra, A., & Araki, T. (2017). Use of spherical elementary currents to map the polar current systems associated with the geomagnetic sudden commencements on 2013 and 2015 St. Patrick's Day storms. *Journal of Geophysical Research: Space Physics*, *122*(1), 194–211. https://doi.org/10.1002/2016JA023166

Marsal, S., Torta, Curto, J. J., Cid, O., & Ibañez, M. (2024). Data-driven transfer functions from differential magnetometer measurements to enhance GIC model validation capability: A case study in the Spanish power grid [Dataset]. *CORA Repositori de Dades de Recerca*. https://doi.org/10.34810/data1741

Matandirotya, E., Cilliers, P. J., Van Zyl, R. R., Oyedokun, D. T., & de Villiers, J. (2016). Differential magnetometer method applied to measurement of geomagnetically induced currents in Southern African power networks. *Space Weather*, *14*(3), 221–232. https://doi.org/10.1002/2015SW001289

McLay, S. A., & Beggan, C. D. (2010). Interpolation of externally-caused magnetic fields over large sparse arrays using spherical elementary current systems. *Annals of Geophysics*, *28*(9), 1795–1805. https://doi.org/10.5194/angeo-28-1795-2010

Parry, H. G., Mann, I. R., Kale, A., Milling, D. K., Clark, C., Cui, R., et al. (2024). Using a differential magnetometer technique to measure geomagnetically induced currents: An augmented approach. *Space Weather*, *22*(7), e2024SW003894. https://doi.org/10.1029/2024SW003894

Pirjola, R., Viljanen, A., Pulkkinen, A., Kilpua, S., & Amm, O. (2005). Ground effects of space weather. In I. A. Daglis (Ed.), *Effects of space weather on technology infrastructure* (pp. 235–256). Springer. https://doi.org/10.1007/1-4020-2754-0_13

Pirjola, R. J., Boteler, D. H., Tuck, L., & Marsal, S. (2022). The Lehtinen--Pirjola method modified for efficient modelling of geomagnetically induced currents in multiple voltage levels of a power network. *Annales Geophysicae*, *40*(2), 205–215. https://doi.org/10.5194/angeo-40-205-2022

Pulkkinen, A., Amm, O., & Viljanen, A., & BEAR Working Group. (2003). Ionospheric equivalent current distributions determined with the method of spherical elementary current systems. *Journal of Geophysical Research*, *108*(A2), 1053. https://doi.org/10.1029/2001JA005085

Torta, J. M., Marcuello, A., Campanyà, J., Marsal, S., Queralt, P., & Ledo, J. (2017). Improving the modeling of geomagnetically induced currents in Spain. *Space Weather*, *15*(5), 691–703. https://doi.org/10.1002/2017SW001628

Torta, J. M., Marsal, S., Ledo, J., Queralt, P., Canillas-Pérez, V., Piña-Varas, P., et al. (2021). New detailed modeling of GICs in the Spanish power transmission grid. *Space Weather*, *19*(9). https://doi.org/10.1029/2021SW002805

Torta, J. M., Marsal, S., Piña-Varas, P., Hafizi, R., Martí, A., Campanyà, J., et al. (2023). Expected geomagnetically induced currents in the Spanish islands power transmission grids. *Space Weather*, *21*(7), 1–19. https://doi.org/10.1029/2023SW003426

Torta, J. M., Marsal, S., & Quintana, M. (2014). Assessing the hazard from geomagnetically induced currents to the entire high-voltage power network in Spain. *Earth Planets and Space*, *66*(1), 1–17. https://doi.org/10.1186/1880-5981-66-87

Torta, J. M., Serrano, L., Regué, J. R., Sánchez, A. M., & Roldán, E. (2012). Geomagnetically induced currents in a power grid of northeastern Spain. *Space Weather*, *10*(6). https://doi.org/10.1029/2012SW000793

Trivedi, N. B., Vitorello, Í., Kabata, W., Dutra, S. L. G., Padilha, A. L., Bologna, M. S., et al. (2007). Geomagnetically induced currents in an electric power transmission system at low latitudes in Brazil: A case study. *Space Weather*, *5*(4), S04004. https://doi.org/10.1029/2006sw000282

Weygand, J. M., Engebretson, M. J., Pilipenko, V. A., Steinmetz, E. S., Moldwin, M. B., Connors, M. G., et al. (2021). SECS analysis of nighttime magnetic perturbation events observed in Arctic Canada. *Journal of Geophysical Research: Space Physics*, *126*(11), e2021JA029839. https://doi.org/10.1029/2021JA029839